Extending the mechanical property regime of laser powder bed fusion Sc and Zr modified Al6061 alloy by manipulating process parameters and heat treatment

Zhiguang Zhu, Zhiheng Hu, Fern Lan Ng, Hang Li Seet, Sharon Mui Ling Nai*

Singapore Institute of Manufacturing Technology (SIMTech), Agency for Science, Technology and Research (A*STAR), 5 Cleantech Loop, #01-01 CleanTech Two Block B, Singapore 636732, Republic of Singapore

* Corresponding author

mail address: zhuzg@njust.edu.cn (Zhiguang Zhu), hu_zhiheng@simtech.a-star.edu.sg (Zhiheng Hu), flng@simtech.a-star.edu.sg (Fern Lan Ng), seet_hang_li@simtech.a-star.edu.sg (Hang Li Seet), mlnai@simtech.a-star.edu.sg (Sharon Mui Ling Nai)

Abstract

Highly dense compositionally modified Al6061 alloys with Sc and Zr were fabricated using the laser powder bed fusion. The as-built Al6061Mod alloy exhibits a bimodal grain size distribution consisting of coarse columnar grains and ultrafine grains, which is tunable by either varying the printing parameters or post-heat treatment. A high laser energy density along with a lower cooling rate, leaving more time for nucleating primary Al_3Sc particles, triggers a higher area fraction of ultrafine grains. The heat treatment-induced evolution of microstructure and mechanical properties is jointly influenced by the size of grains and $(Al,Si)_3(Sc,Zr)$ particles. The conventional T6 heat treatment triggers coarsening of grains (~5.3 μm) and $(Al,Si)_3(Sc,Zr)$ particles (~42 nm), lowering the yield strength (~280 MPa) compared with that of as-built counterparts. On the contrary, direct aging enhances the yield strength (~383 MPa) due to the precipitation of nano-sized secondary $Al_3(Sc,Zr)$ particles (~5 nm) as well as retaining the grain size (~690 nm) of ultrafine grains. Concurrent with the tunable strength, the plasticity behaviors (Lüders band and Portevin-Le Chatelier effect) are manipulated correspondingly with varying microstructure. The broad tailoring of microstructure and mechanical property regime can shed light on designing Al alloys targeting the desired applications by manipulating the printing parameters and heat treatment.

Keywords: Laser powder bed fusion; Aluminum alloy; Heat treatment; Microstructure; Mechanical property.

1. Introduction

Laser powder bed fusion (L-PBF) can construct the three-dimensional (3D) components in a layer-by-layer manner boasting the advantages of low tooling cost and unlimited design freedom [1]. In analogy to the micro-welding process, the L-PBF has been broadly implemented to fabricate a variety of weldable alloys, such as the Ti alloys [4], stainless steels [6], and Ni-based superalloys [7]. While for the alloys with a poor weldability, such as high-strength Al alloys [9-12] (Al–Cu-based 2xxx series alloys [9], Al–Mg–Si-based Al6xxx series alloys [11], and Al–Zn–Mg-based Al7xxx series alloys [12]), the formation of hot cracks deteriorates the mechanical performance and impedes the industrial applications. The harsh demand for weldability for the printable alloys has limited the Al alloy systems amenable for L-PBF to Al–Si–(Mg) series alloys [13-19], which in turn hinders the L-PBF from maturing to its full potential for Al alloys.

To eliminate the crack issues during L-PBF, the common solutions are assisted by tailoring the processing methods to alter the solidification conditions (such as thermal gradient and solidification velocity) [20] or composition modification to enhance the heterogeneous nucleation [21,22]. The general philosophy of process tailoring is to decrease the thermal gradient, residual stress, or solidification velocity [23]. It is reported that powder bed heating at 500 ˚C can eliminate the cracks during L-PBF processing of Al6061 alloy [20]. However, this method is not universal and highly depends on the machine. As for the composition modification, the basic principle is to introduce the elements that can trigger the formation of Al_3X (X= Zr, Sc, Nb, or Ta) nanoparticles with low lattice misfit with the Al matrix [24-31]. The low lattice misfit between the Al_3X particles and Al matrix ensures the low interfacial energy for the heterogeneous nucleation, enabling the formation of ultrafine grains (UFGs) and the elimination of cracks. This inoculation treatment design concept has been verified in numerous high-strength Al alloys and applied to develop other high-performance alloys beyond Al alloys [32].

With the inoculation treatment method, crack-free high-strength Al alloys are fabricated, some of which have been commercialized, such as the Scalmalloy® [33], and 7A77.60 [34], leading to a research hotspot for novel high-strength Al alloys. The Al6xxx (Al–Mg–Si) series alloys are considered to be the most promising candidates for aluminum automotive body panel applications [35]. As a typical Al6xxx alloy, the Al6061 alloy has a variety of industrial applications due to its high specific strength, excellent corrosion resistance, and high thermal/electrical conductivity [36]. Recently, significant progress has been achieved in eliminating the cracks during L-PBF of Al6061 alloys. Mehta et al. [11] and Opprecht et al. [30,37] have fabricated the crack-free Al6061 alloy with a heterogeneous microstructure via the inoculation treatment of Zr and Yttrium Stabilized Zirconia (YSZ), respectively. The grain microstructure and crack behaviors can be controlled by the content of added inoculation treatment powders. Increasing the content of inoculation treatment powders can effectively enhance the area fraction of UFGs. However, these works mainly focused on the printing feasibility for crack-free samples, while tailoring the microstructure and mechanical properties is seldom mentioned except for varying the content of inoculation-treated powders. Since the printing parameters, such as the laser power and scanning speed, can affect the thermal gradient and solidification velocity [38], it is necessary to explore the "printing parameter−microstructure−mechanical property" relationship to optimize the microstructure for the target applications besides the composition modification. Moreover, due to the composition modification and the special processing characteristics (such as the rapid cooling rate and thermal cycling) associated with L-PBF, the appropriate heat treatment for L-PBF Al6061 alloy rather than the conventional T6 heat treatment might need to be designed to yield high mechanical performance.

Apart from crack healing, the specific microstructure arising from the layer-by-layer construction and non-equilibrium solidification, which is not easily attained via conventional processing, can also provide a model platform to investigate scientific issues, such as the Lüders band, which is normally observed for the L-PBF Al alloys containing the UFGs. However, the investigation on the evolution of the Lüders band caused by varying the processing parameter and heat treatment effect is scarce. Moreover, due to the formation of thermally stable $Al_3(Sc,Zr)$ particles for the Sc- and Zr-modified Al alloys, it has potential high-temperature applications [39]. However, most of the studies focus on room-temperature tensile properties, while the study on high-temperature tensile properties is scarce [40].

To fill the gap, a compositionally modified Al6061 alloy with Zr and Sc amenable for L-PBF was designed and selected as a model system to understand the following issues: (1) To uncover the printing parameter effect, by tailoring the laser energy density, on the microstructure evolution and its consequence on the mechanical property; (2) Various heat treatment profiles are adopted to investigate their effects on the microstructure and tensile property; and (3) High-temperature tensile properties of the L-PBF Sc- and Zr-modified Al6061 alloy.

2. Experiment

2.1 Powder characteristics

The studied alloy is Al6061 alloy modified with Sc and Zr, which will be called as Al6061Mod in this paper. Gas atomized powders with a composition of Al-0.96Mg-0.64Si-0.52Sc-0.28Cu-0.26Zr-0.24Cr-0.08Fe (wt.%, as measured by inductively coupled plasma atomic emission spectroscopy, ICP-AES) were used for the L-PBF process [42]. The gas-atomized powders mainly exhibit spherical morphology with some satellites attached to the surface. The particle size distribution measured via the Mastersize 3000 indicates that the d_{50} of the powders is 39.4 ± 1.4 µm.

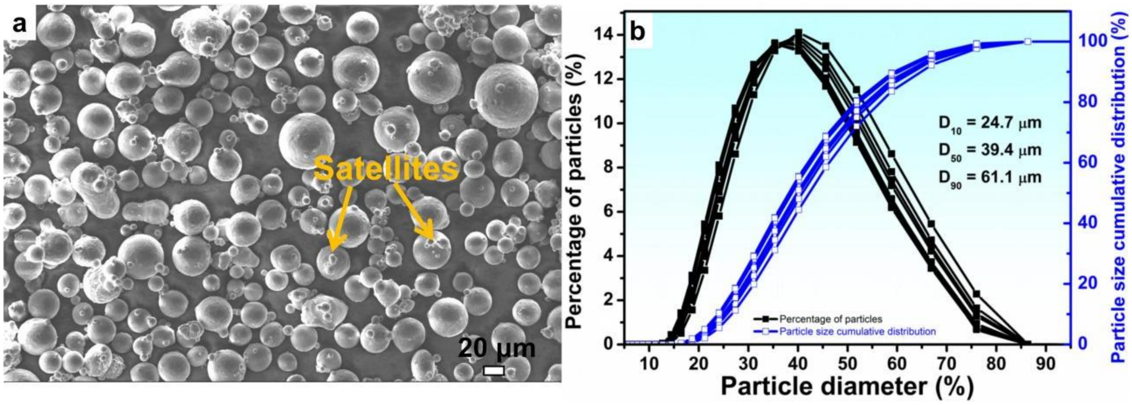

Fig. 1 (a) SEM image and (b) particle size distribution of the Al6061Mod powders.

2.2 L-PBF printing process and densification characterization

All the L-PBF processes were conducted using a ProX DMP 300 (3D systems, US) equipped with a 500 W fiber laser and a laser beam diameter of 75 μm. The chamber was purged with argon to ensure that the oxygen level was below 300 ppm. The scanning strategy is the same as our previous work [43] with a rotation angle of 90° between adjacent layers. The laser powder (p), layer thickness (t), and hatching space (h) were kept constant, while the scanning speed (v) was varied to optimize the printing process and tailor the microstructure. The adopted scanning speeds were 100, 200, 400, 800, and 1800 mm/s, and the corresponding laser volumetric energy density, $E = P/hvt$, were 1188, 594, 297, 149, and 66 J/mm^3, which were labelled as E1188, E594, E297, E149, and E66, respectively. There was no significant composition variation after L-PBF, and the chemical composition of the as-built sample with E297 was Al-0.96Mg-0.65Si-0.53Sc-0.28Cu-0.27Zr-0.24Cr-0.10Fe (wt.%). To evaluate the relative density, the optical microscopy (OM) images were analyzed via ImageJ software [25,44,45]. The OM images were firstly binarized and then the fraction of pores was measured by applying a threshold, which is exemplified in Fig. S1 in the Supplementary Information (SI). Ten areas covering an area of approximately 696 × 522 μm^2 randomly distributed in the cross-section of the sample were selected for OM analysis. Three kinds of samples were printed: (1) cubic samples with a dimension of 10 mm × 10 mm × 10 mm for optimizing the printing process; (2) cuboid samples with a dimension of 80 mm (length) × 10 mm (width) × 10 mm (height) for the tensile test along the horizontal direction perpendicular to the building direction; (3) cuboid samples with a dimension of 20 mm (length) × 10 mm (width) × 45 mm (height) for the tensile test along the vertical direction parallel to the building direction.

2.3 Heat treatment details

The heat treatment (HT) of the Al6061Mod specimens was performed in a muffle furnace. The thermocouple was touched with the sample to ensure the temperature accuracy during heat treatment. In the present work, two heat treatment profiles were adopted to tailor the microstructure and explore its consequences on the mechanical properties. One is the conventional T6 heat treatment adopted for the Al6061 alloys, which includes two steps, solution treatment at 530 °C for 5 h followed by water quenching. The water-quenched samples were then aged at 175 °C for 8 h. The other heat treatment is direct aging by annealing the as-printed samples at a certain temperature, viz, 300, 350, 400, and 450 °C, respectively. After direct aging, the samples were taken out of the furnace and cooled in the air.

2.4 Microstructural analysis

The densification of L-PBF Al6061Mod samples was characterized using optical microscopy (OM). To unveil the laser scanning pattern and melt pool boundary, the as-printed samples were etched using Keller's reagent (95.0 vol.% H_2O + 2.5 vol.% HNO_3 + 1.5 vol.% HCl + 1 vol.% HF) solution. The microstructure of specimens was characterized using field emission scanning electron microscopy (FESEM) (JEOL JSM 7600) and electron backscattered diffraction (EBSD). The SEM and EBSD samples were ground mechanically with silicon carbide sandpapers and subsequently polished with 0.3 μm diamond suspensions and 40 nm oxide polishing suspensions (OPS). The EBSD was performed in a Zeiss Ultra Plus FESEM and the EBSD data was analyzed using AZtecCrystal software. High-resolution high-angle annular dark field (HAADF), scanning TEM (STEM), and energy dispersive X-ray spectroscopy (EDS) were conducted using an FEI F200X Talo S/TEM operated at 200 kV. TEM foils were mechanically ground to a thickness of ~ 50 μm, which were subsequently ion milled using a Precision Ion-Polishing System Gatan 691.

2.5 Mechanical properties

The hardness values of as-built and heat-treated Al6061Mod specimens were measured using the Vickers hardness test with a load of 100 grams for 15 s. The rectangular dog-bone-shaped tensile specimens with a gauge dimension of 12.5 mm × 3.2 mm × 1.6 mm were machined from the block samples by the electrical discharge machining (EDM). It is noted that the length of the clamping end of the tensile samples along the horizontal and vertical directions is different. The room temperature and elevated temperature tensile tests were performed using a universal Instron-5982 testing system equipped with an automated video extensometer to measure the displacement of the gauge section precisely. The strain rate of the tensile test is 10^{-3}/s. For the high-temperature tensile test at 150, 200, and 240 °C, the samples were heated to the testing temperature and soaked for 20 mins to reach the heat equilibrium before commencing the test.

3. Results

3.1 Densification and microstructure of the as-built sample

Based on the OM image analysis method, the relative density is 99.45%, 99.61%, 99.92%, 99.94%, and 99.45%, respectively for E1188, E594, E297, E149, and E66 samples. The typical 2D (Fig. S2a in the SI) and 3D OM (Fig. S2b in the SI) images of the L-PBF E297 sample imply that highly dense and crack-free samples can be fabricated when printed with E297. This is different from L-PBF Al6061 alloy, which exhibits a significant cracking under all the laser energy densities based on the literature [11,30,46]. Figure 2 shows the multi-scale microstructure of E297 using the SEM and EBSD. Figures 2a-e show the effect of laser energy density on the microstructure evolution of the as-built Al6061Mod alloy. All the samples exhibited a bimodal grain structure with coarse columnar grains (CCGs) (Fig. 2c_1) in the center of melt pools and UFGs along the melt pool boundary (Fig. 2c_2), which contrasts with that of L-PBF Al6061 with coarse columnar grains growing along the building direction [11]. A similar bimodal grain structure has also been observed for the Zr-modified Al6061 alloy [11,47]. The width of the CCGs ranges from 1.0 μm to 5.9 μm, while the length of CCGs was from 3.6 μm to 16.4 μm for the E297 sample (Figs. 2c and c_1). In contrast, the average grain size of equiaxed grains is about 690 nm for the E297 sample (Fig. 2c_2). There is a trend that the area fraction of UFGs decreased with decreasing laser energy density, which decreases from ~71.5% (E1188) to ~33.8% (E66). The SEM images (Figs. 2f, f_1, and f_2) further confirm the formation of a heterogeneous microstructure, and the white-contrasted phases can be observed in both the columnar and equiaxed grains.

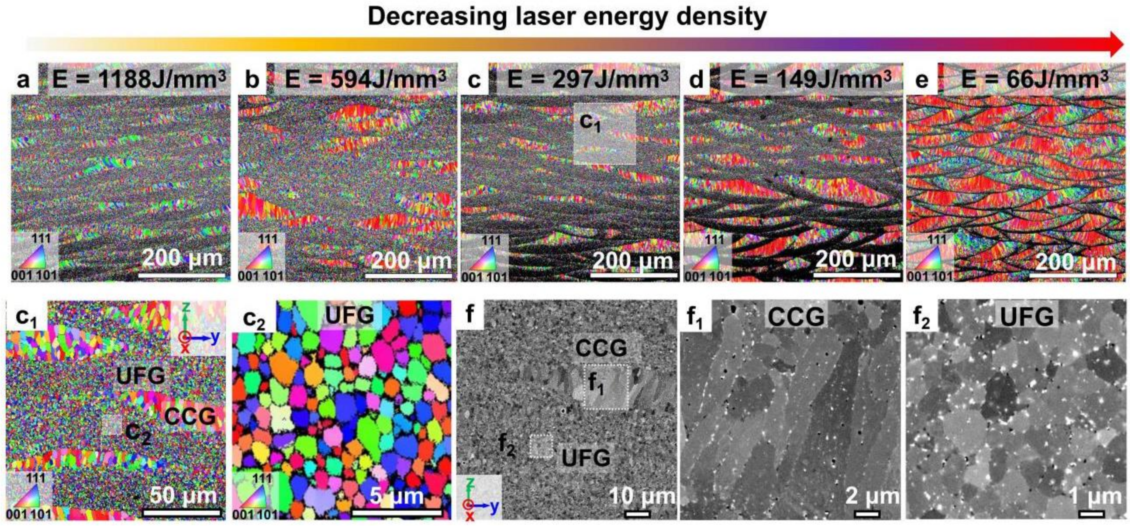

Fig. 2 Microstructure of the as-built Al6061Mod alloy. EBSD of the samples under different laser energy densities: (a) E = 1188 J/mm^3, (b) E = 594 J/mm^3, (c) E = 297 J/mm^3, (d) E = 149 J/mm^3, (e) E = 66 J/mm^3. (c_1) and (c_2) EBSD of E297 sample at higher magnifications. (f,f_1,f_2) SEM images showing the heterogeneous microstructure and formation of white-contrasted precipitates in the E297 sample.

To gain a deeper understanding of the microstructure of the as-built Al6061 Mod sample, the TEM was adopted to analyze the precipitates. Figure 3 shows the bright (BF)/ HAADF and the corresponding energy dispersive spectrum (EDS) mapping images of the UFGs (Figs. 3a, 3b, 3a_1-a_8) and CCGs (Figs. 3c, d, c_1-c_{10}) in the as-built E297 sample. The findings are listed below:

(1) Mg/Si-enriched phase with size ranging from ~40 nm to ~120 nm, most likely to be the Mg_2Si phase, formed to decorate along the boundary of both the UFGs (Figs. 3a_2, a_3) and CCGs (Figs. 3c_2, c_3). Additionally, Fe-enriched precipitates tend to form in the adjacent Mg/Si-enriched dispersoids [30,48] in both the UFG (Fig. 3a_4) and CCG (Fig.

3c4) regions. This is perhaps due to the co-precipitation of Mg/Si-enriched precipitates and Fe-enriched precipitates.

(2) Sc-enriched particles were detected in the interior and boundary of UFGs (Fig. 3a6), while no obvious Zr enrichment was detected along these Sc-enriched particles (Fig. 3c6). Notably, evidence of Sc-enriched particles could also be detected in the CCG (Fig. 3c6).

(3) Several oxides were observed in the CCGs (Fig. 3c8), which are the possible Mg oxides.

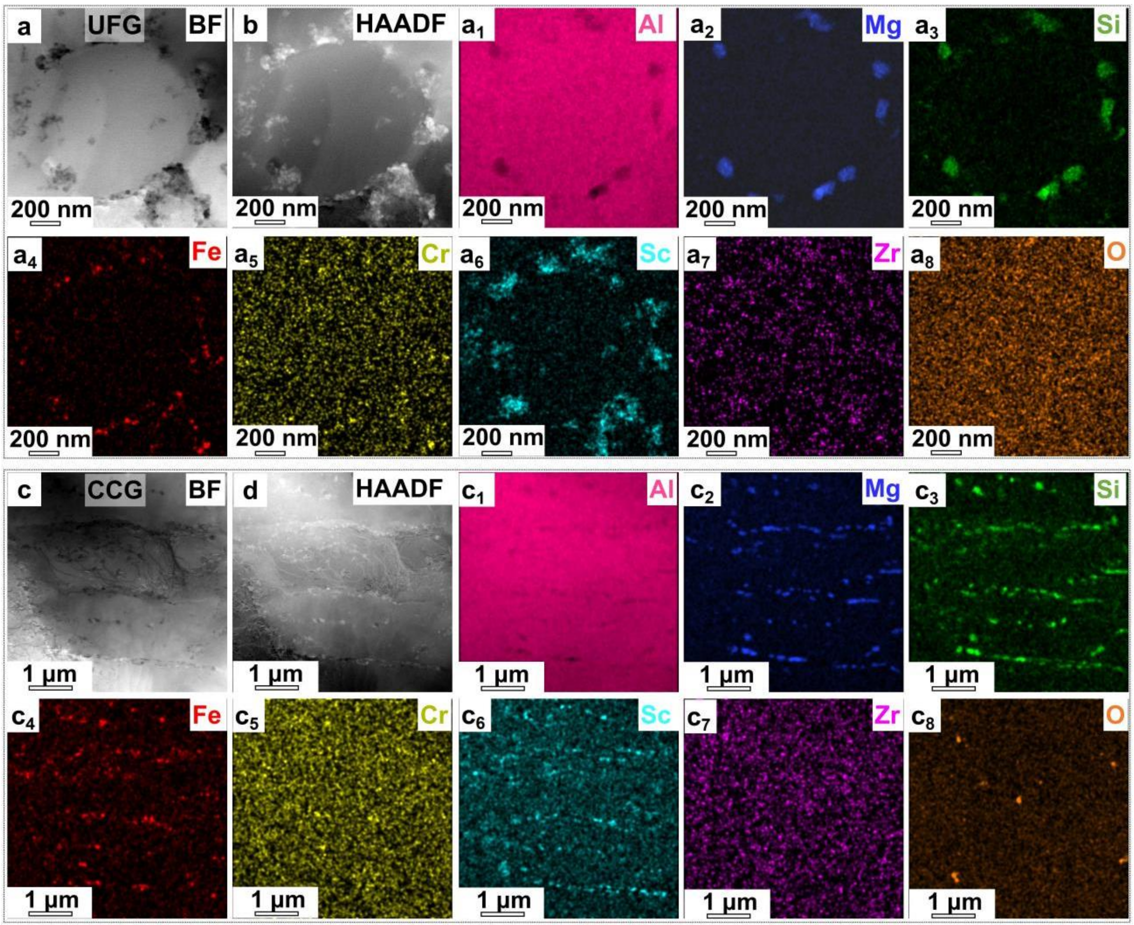

Fig. 3 STEM analysis of the UFGs and CCGs in the as-built sample. (a) BF and (b) HAADF images of UFGs. (a_1)-(a_8) show the corresponding EDS mapping images of the (a). (c) BF and (d) HAADF images of CCGs. (c_1)-(c_8) show the corresponding EDS mapping images of the (a_1).To further characterize the structure of Sc-enriched precipitates, the microstructure characterizations were conducted based on selected area diffraction (SAED) patterns and HRTEM. The SAED pattern was taken along the [001]

zone axis, showing the super-lattice reflections from the $L1_2$-structured phase (Fig. 4a). Figure 4b shows the HRTEM image presenting the Al matrix and Al_3Sc, whose $L1_2$ structure is supported by the inset Fast Fourier Transformation (FFT). Figure 4c shows the interfacial coherence between the Al matrix and Al_3Sc.

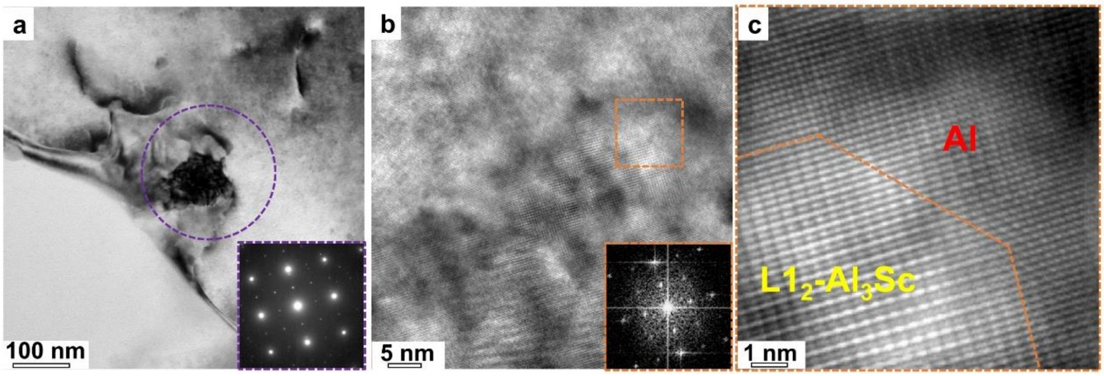

Fig. 4 TEM image of as-built Al6061Mod sample. (a) TEM image taken from the UFGs showing the Al_3Sc particle, as reflected by the circle. The inset shows the selected area diffraction pattern of the circled precipitate along [001] showing the superlattice reflections. (b) HRTEM image taken along the [001] zone axis. The inset shows the Fast Fourier Transformation (FFT) of the corresponding rectangular area. (c) HRTEM image showing the interface between Al and Al_3Sc.

3.2 Heat treatment effect on the microstructural evolution

3.2.1 Selection of heat treatment profiles

The following section studies the dependence of microstructure evolution on the heat treatment profiles for the E297 sample. Two heat treatment profiles were adopted. One is the T6 consisting of solution treatment (ST) at 530 °C for 5 h followed by aging at 175 °C for 8 h. The other is direct aging at 300, 350, 400, and 450 °C. Figure 5 shows the hardness evolution of the as-built Al6061Mod under various heat treatment conditions. The hardness increased marginally from 103.6 HV in the as-built state to about 108.3 HV after T6 heat treatment. As for DA, the dwelling temperature plays a significant role in influencing the hardness evolution. With the lowest DA temperature adopted in the present study (300 °C), the hardness experienced a minor drop to about 93.8 HV after aging for 5 mins, which might be associated with the annihilation of dislocations [49]. Then it increased to the peak value of about 124 HV after aging for 8 h and kept constant with the prolonged aging. Upon aging at 350 °C, the microhardness increased to the peak value of about 124 HV for 4 h, and it remained at a similar level upon further aging. When directly aged at 400 and 450 °C, the microhardness increased to the peak value of 123 HV and 117 HV for 1 h and 10 min, respectively. The shorter time to reach the peak hardness signifies the accelerated precipitation kinetics at higher temperatures [31,50,51]. The heat treatment conditions of T6 and DA at 350 °C for 4 h were studied in the following to understand the dependence of heat treatment on microstructure and mechanical properties.

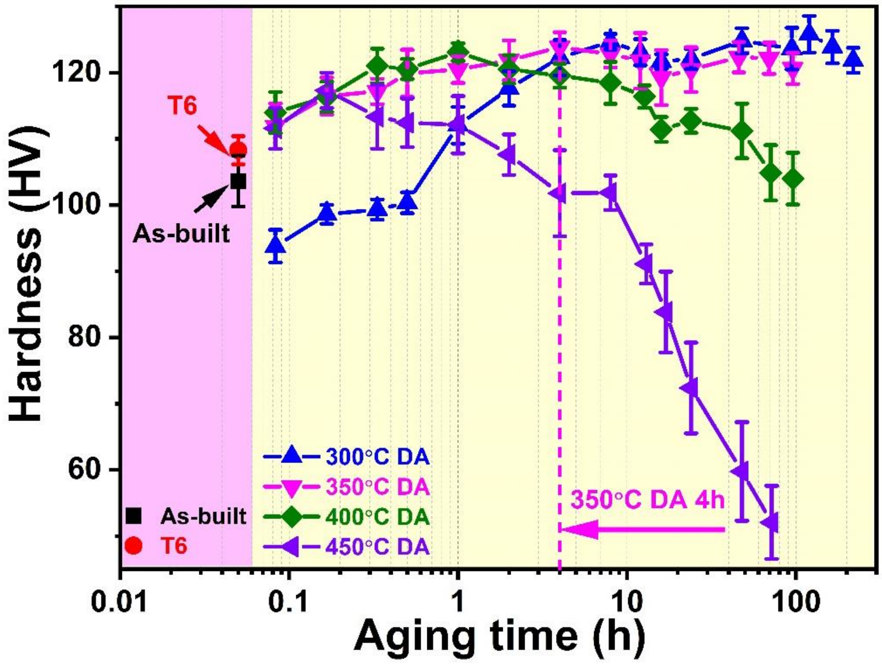

Fig. 5 The microhardness evolution of as-built Al6061Mod under various heat treatment conditions.

3.2.2 T6

The 3D OM image (Fig. 6a) shows that the melt pools become inconspicuous after T6 heat treatment. The SEM (Figs. 6b-d) and EBSD (Figs. 6e-g) indicate that the grains undergo significant coarsening to an average grain size of about 5.3 μm (Fig. 6h). White-contrasted precipitates are observed in the interior of grains and along grain boundary (Figs. 6c and d). The EDS mapping (Figs. 6g$_1$-g$_3$) of the corresponding area in Fig. 6g indicates the presence of Sc and Zr-enriched precipitates. To further confirm the precipitates associated with T6 heat treatment, Fig. 7 presents the STEM-EDS mapping of the as-built Al6061Mod after T6. Fe-Cr-enriched (Figs. 7a$_4$ and a$_5$) and Sc-Zr-enriched (Figs. 7a$_6$ and a$_7$) particles were detected. Si tends to co-precipitate with the Fe-Cr-enriched and Sc-Zr-enriched particles. In another region, the Mg-Si-enriched particles were observed besides the Fe-Cr-Si-enriched and Sc-Zr-Si-enriched particles (Fig. S3 in the SI). Moreover, the co-precipitation of Fe-Cr-Si-enriched phase (Figs. 7a$_5$, a$_6$ and a$_7$) and Sc-Zr-Si-enriched phase (Figs. 7a$_3$, a$_6$ and a$_7$) were observed. Furthermore, the Mg-Si-enriched phase (Figs. 7a$_2$ and a$_3$) was observed to precipitate attaching to the surface of Fe-Cr-Si-enriched and Sc-Zr-Si-enriched particles. Finally, the SAED result (Fig. 7d) of Sc-Zr-Si-enriched particles (Figs. 7c, c$_1$, c$_2$, c$_3$) indicateds it still retains the L1$_2$ structure. The Sc-Zr-Si-enriched precipitates with an average diameter of ~42 nm are possible $(Al,Si)_3(Sc,Zr)$ particles [52]. At the nanoscale, Mg-Si-enriched phases were observed (Figs. 7e, e$_1$, e$_2$, and f) with two different morphologies. The lath-shaped particles are the possible L phase which was observed for the Cu-containing Al-Mg-Si alloy [53]. In contrast, the rod-shaped precipitates are possibly the β' and β'' phases during aging [54]. The detailed analysis of Mg-Si-enriched precipitates for T6 Al6061Mod deserves further investigation.

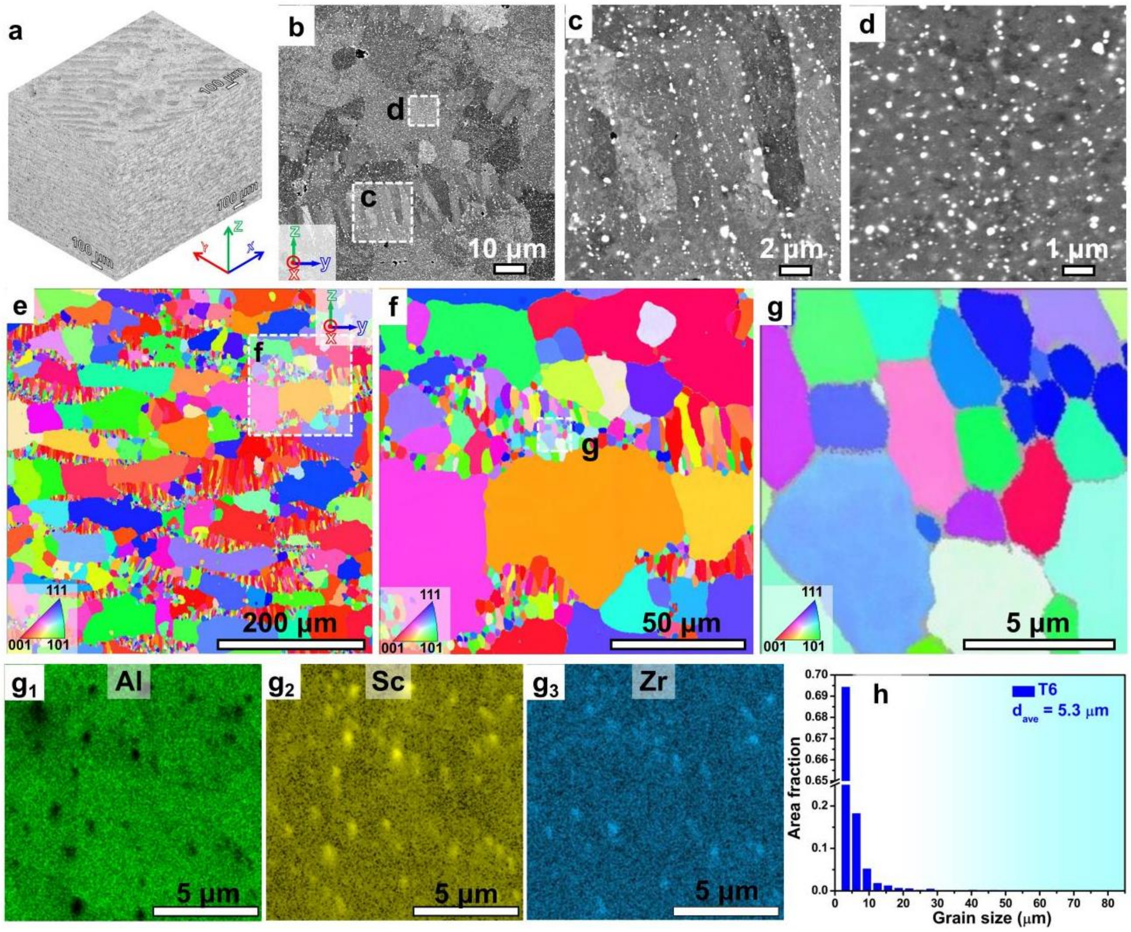

Fig. 6 Microstructure of the as-built Al6061Mod alloy after T6. (a) 3D OM image shows a high densification. (b-d) SEM images showing the heterogeneous microstructure and formation of white-contrasted precipitates. (e-g) EBSD images showing the grain size distribution. (g_1-g_3) EDS elemental mapping of the corresponding area in (g). (h) Grain size distribution of the T6 Al6061Mod sample.

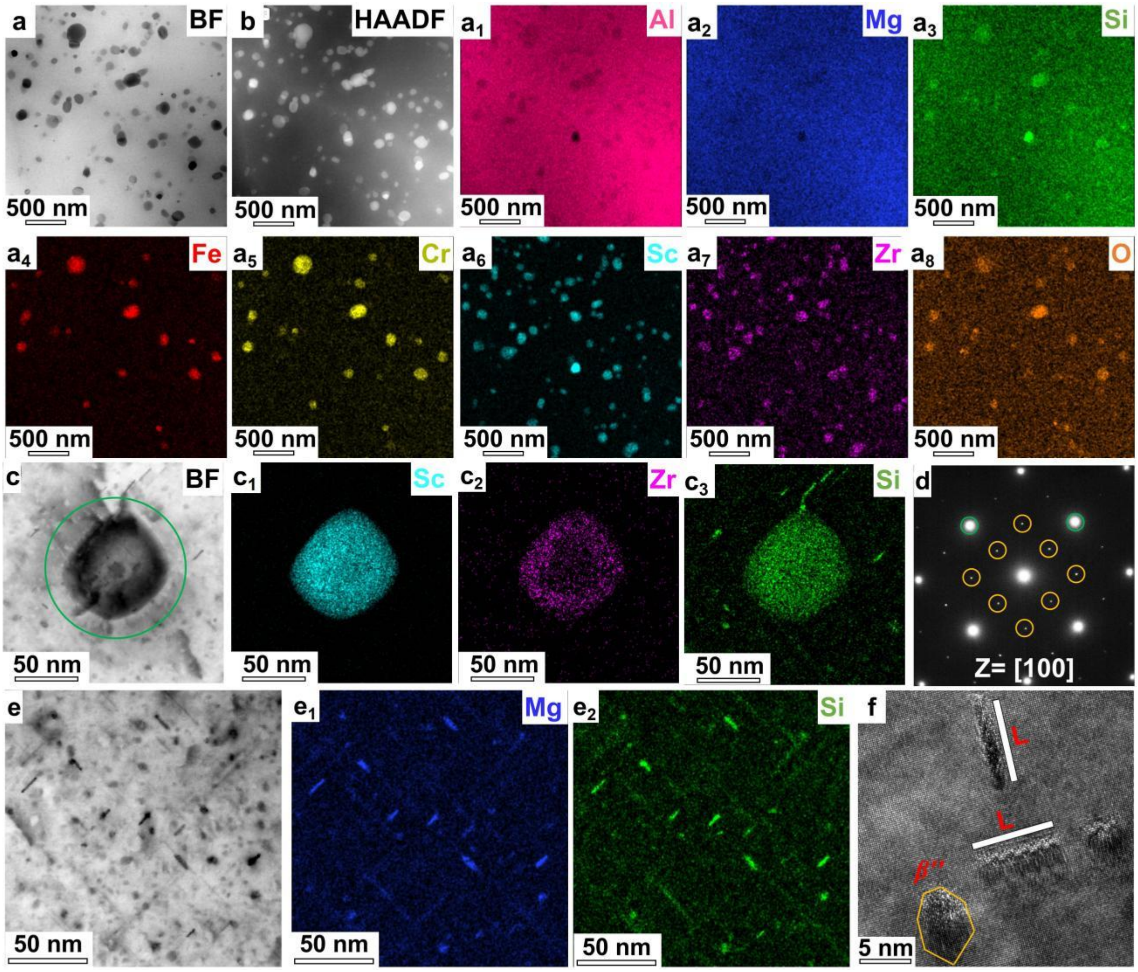

Fig. 7 STEM microstructural characterization of the as-built Al6061Mod alloy after T6. (a) BF and (b) HAADF image of the samples. (a_1-a_8) STEM EDS mapping of the corresponding area in (a_2). (c) BF, (c_1-c_3) EDS mapping, and (d) SAED of Sc-Zr-Si-enriched particle. (e) BF, (e_1,e_2) EDS mapping, and (f) HRTEM image of the Mg-Si-enriched precipitates.

3.2.3 DA

Figure 8 presents the microstructure after DA at 350 °C/4 h. In contrast to the T6 samples, the heterogeneous microstructure with a multimodal grain size distribution remains intact (Figs. 8a-d). The grain size undergoes quite a marginal coarsening, and the average grain size of UFGs, d_{ave}, was about 690 nm (Fig. 8e), similar to that in the as-built condition. Besides, evidence of Sc-rich precipitates was obvious based on the EBSD observation scale (Figs. 8c_1, c_2, and c_3).

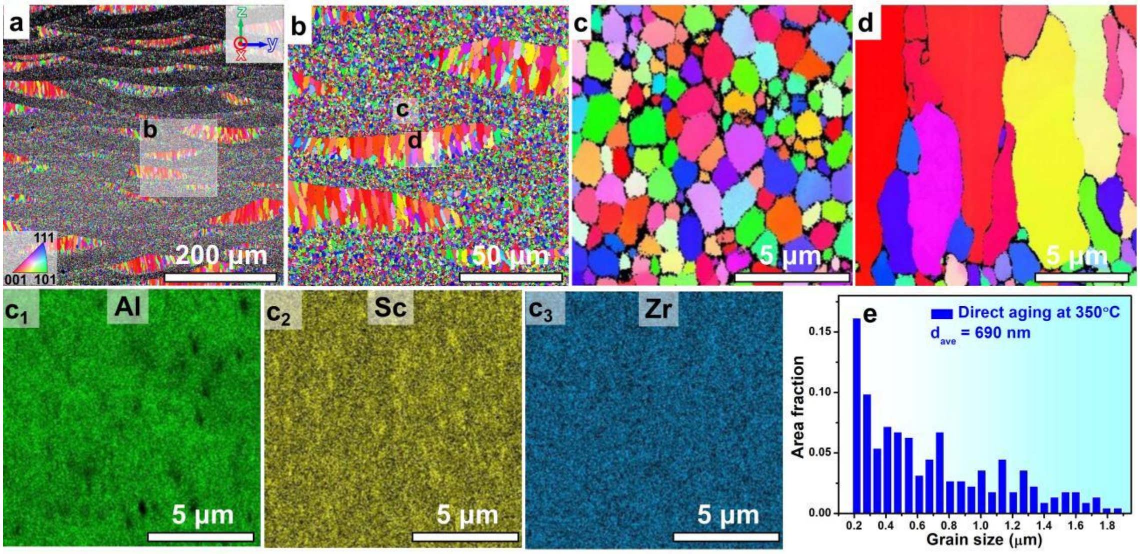

Fig. 8 Microstructure of the as-built Al6061Mod alloy after DA at 350 ˚C/4 h. (a-d) EBSD images showing the existence of heterogeneous microstructure with multimodal grain size distribution. (c_1-c_3) The EDS mapping of the corresponding area in c. (e) Grain size distribution in the ultrafine grain region.

To gain a deeper understanding of the microstructure evolution at the nanoscale after DA, Fig. 9 shows the STEM and EDS mapping images of the UFGs. Mg-Si-enriched (Figs. 9a_2 and a_3), Fe-enriched (Fig. 9a_4), and Sc-enriched (Fig. 9a_6) particles could be observed. These Mg-Si-enriched particles are possibly Mg_2Si particles. The HAADF STEM imaging performed along the <001> zone axis presents the circled $Al_3(Sc,Zr)$ particles with a diameter of ~5 nm (Fig. 9c). These secondary $Al_3(Sc,Zr)$ particles are coherent with the Al matrix (Fig. 9d).

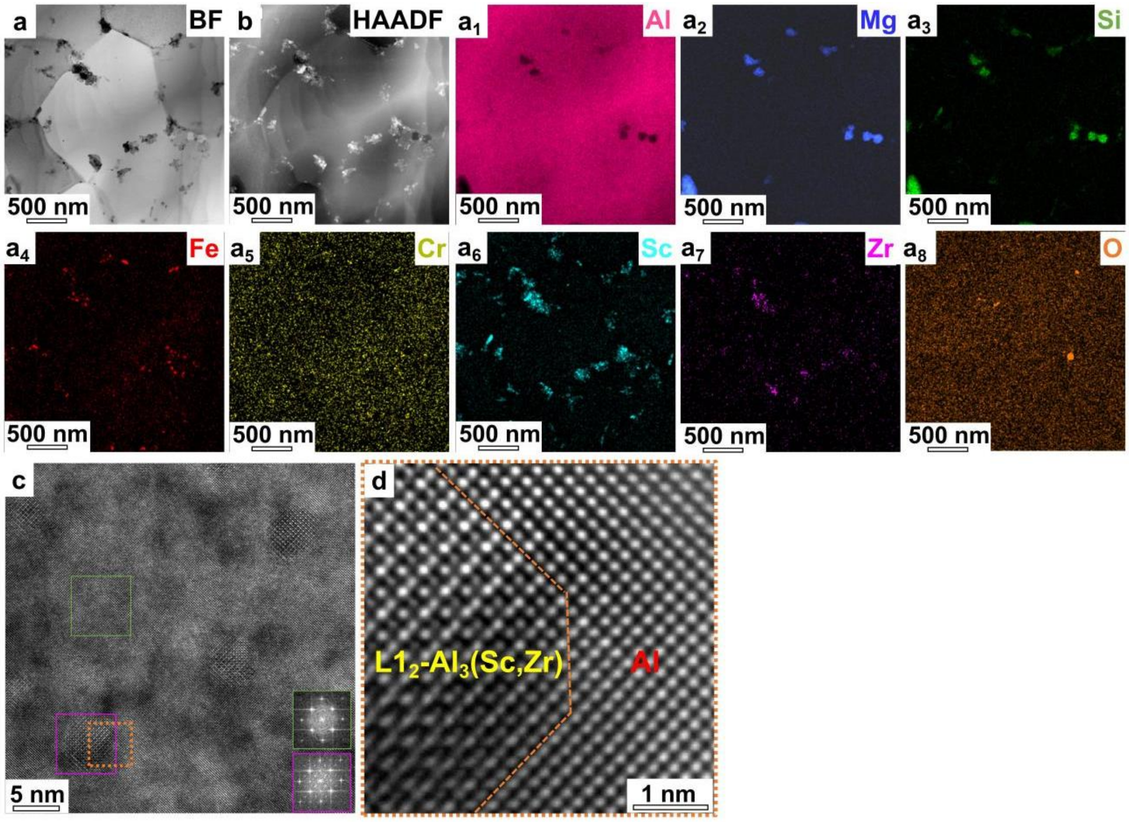

Fig. 9 STEM and EDS mapping of the as-built Al6061Mod alloy after DA. (a) BF, (b) HAADF, (a_1-a_8) EDS mapping of the as-built Al6061Mod alloy. (c) HAADF-STEM image showing the $L1_2$-structured $Al_3(Sc,Zr)$ particles. (d) Magnified area in (c) showing the atomic coincidence across the interface between the Al matrix and $Al_3(Sc,Zr)$.

3.3 Heat treatment effect on the evolution of mechanical properties

3.3.1 Tensile property evolution under heat treatment

The tensile properties of L-PBF Al6061Mod alloy under different processing and heat treatment conditions were systematically explored. The values of tensile properties are listed in Table 1. Figure 10a shows the tensile properties of the horizontally- and vertically-built E297 sample. The yield strength (σ_y) is ~325 MPa with an elongation to fracture (ε_f) of ~21.1% for the horizontal samples, while it is ~286 MPa and 18.3% for the vertically-built sample. Both the σ_y and ε_f are higher than those of wrought Al6061 counterparts, which are 276 MPa and 12%, respectively [55]. During tension, the stress drops after yielding followed by a deformation plateau, which is due to activation of the Lüders band with a total of ~9.3%. Subsequently, there is a marginal work hardening till fracture. Figure S4 in the SI shows an OM image of the sample deformed to ~4.2%, which presents the heterogeneous deformation behavior. The surface of the deformed region is characterized by the deformation bands while it is unobvious in the undeformed region. Figure 10b demonstrates the effect of printing parameters on the tensile properties. The E594 sample shows a relatively lower σ_y yet a higher ε_f compared to those E297 counterparts. For the E66 sample, the ε_f was not consistent due to the existence of a lack of fusion defects (Fig. S5 in the SI). In the meanwhile, the Lüders strain of ~5.7% is lower for the E594 sample relative to that of the E297 sample, and the E66 sample exhibits the lowest Lüders strain of ~4.5%. Figure 10c shows the tensile properties of the as-built E297 sample under various heat treatment conditions. To rule out the influence of natural aging on the tensile property, the tensile test was commenced immediately after quenching to water for the solution-treated (ST) samples. The ST samples exhibit a lower σ_y of ~111 MPa and the Lüders band reflected by the deformation plateau disappears. In the meanwhile, the Portevin-Le Chatelier (PLC) effect reflected as the jerky flow is observed in the ST samples [56]. After T6, the σ_y is enhanced to ~280 MPa with the absence of jerky flow. The DA at 350 ˚C/4 h yields the highest σ_y of ~ 383 MPa yet undergoes strain softening with no evidence of work hardening after yielding. The work softening leads to an ε_f of ~5.5%. To study the natural aging effect on the tensile property of ST specimens, Figure 10d indicates the tensile properties of ST Al6061Mod samples that were naturally aged at room temperature for different periods. After natural aging at room temperature for 15 days, the yield strength increases by ~71% to ~191 MPa and the jerky flow due to the PLC effect disappears [57]. When the natural aging time further proceeds to 30 days, the increase of yield strength is marginal to ~201 MPa, indicating that the natural aging for 15 days almost reaches the saturated level.

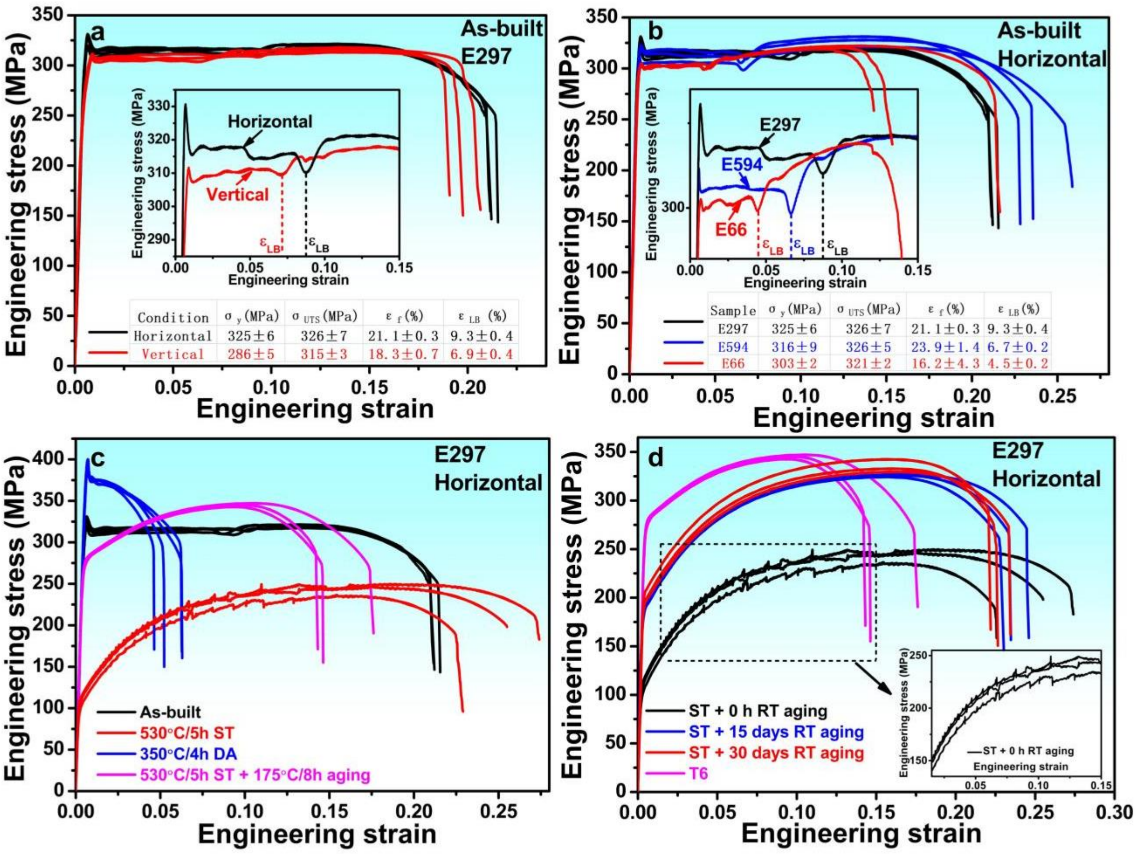

Fig. 10 Tensile properties of the as-built Al6061Mod alloy under various conditions. (a) Tensile properties of as-built Al6061Mod sample along the horizontal and vertical directions. The inset image shows the evolution of Lüders band under these two conditions. The yield strength, ultimate tensile strength, elongation to fracture, and Lüders band strain were listed in the inset. (b) Laser energy density effect on the tensile properties of as-built Al6061Mod sample. The inset image shows the evolution of Lüders band under different laser energy densities. The yield strength, ultimate tensile strength, elongation to fracture, and Lüders band strain were listed in the inset. (c) Heat treatment effect on the tensile property of as-built Al6061Mod alloy with E297. (d) Natural aging effect on the tensile properties of the as-built Al6061Mod alloy after solution treatment.

The high-temperature tensile properties of the E297 sample under different heat treatment conditions are shown in Fig. 11a. The σ_y decreases to ~ 200 MPa and ~ 172 MPa when the testing temperature increases to 200 and 240 °C, in conjunction with an increase of ε_f to ~30.5% and 33.7%, respectively, for the as-built Al6061Mod. Though the DA specimen exhibited a higher σ_y relative to that of as-built samples, the σ_y is similar when tested at 200 °C. In the meantime, the DA Al6061Mod exhibited a poorer ductility relative to that of the as-built sample when tested at 200 °C. The insignificant enhancement of yield strength after DA is also reported in an Al–Cu–Ce(–Zr) alloy [58]. The high-temperature tensile properties of the present alloy were benchmarked with those of AlSi10Mg [59], Al–10Ce–8Mn [60], Al–10.5Ce–3.1Ni–1.2Mn [61], Al–5.7Ni [62], and AA8009 [63] (Figs. 11b-d). It can be observed that the as-built Al6061Mod exhibits a higher yield strength relative to that of workhorse AlSi10Mg alloy and a creep-resistant Al–10.5Ce–3.1Ni–1.2Mn alloy [61]. However, there is much room for improvement in strength as compared with that of AA8009 alloy.

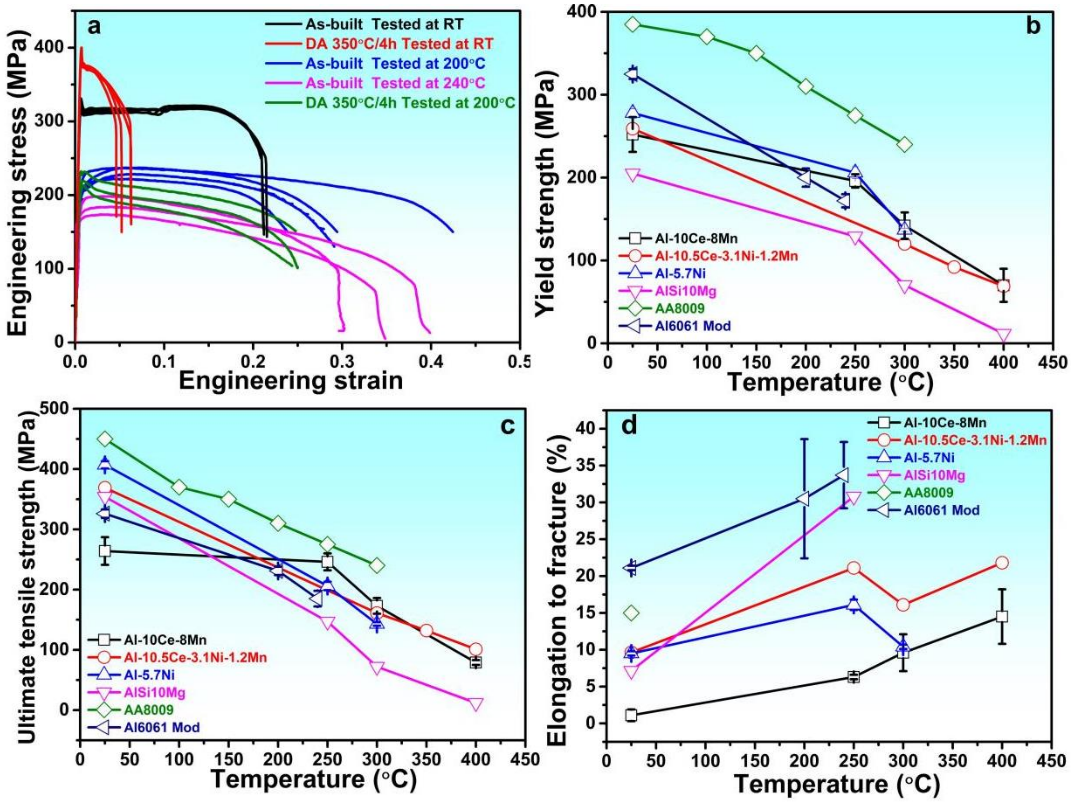

Fig. 11 (a) High-temperature tensile property of Al6061Mod alloy. (b) Yield strength, (c) ultimate tensile strength, and (d) elongation to fracture benchmarked with those of other Al alloys, including the AlSi10Mg [59], Al–10Ce–8Mn [60], Al–10.8Ce–3.1Ni–1.2Mn [61], Al–5.7Ni [62], and AA8009 [63].

Table 1: Tensile properties of the Al6061Mod alloy under different processing and heat

treatment conditions. In the direction column, H (V) stands for horizontal (vertical) direction, indicating that the loading direction is perpendicular (parallel) to the building direction. σ_y: Yield strength, σ_{UTS}: Ultimate tensile strength, ε_f: Elongation to fracture, ε_{LB}: Strain of Lüders band. $\Delta\sigma$: Difference between σ_{UTS} and σ_y, to reflect the work hardening ability. The mechanical properties of the wrought Al6061 sample
are cited from Ref. [55].

Sample	Condition	Temperature (°C)	Direction	σ_y (MPa)	σ_{UTS} (MPa)	ε_f (%)	ε_{LB} (%)	$\Delta\sigma$ (MPa)
E297	As-built	RT	H	325±6	326±7	21.1±0.3	9.3±0.4	1
			V	286±5	315±3	18.3±0.7	6.9±0.4	29
		200	H	200±11	231±7	30.5±8.1	-	31
		240	H	172±8	185±13	33.7±4.5	-	13
	DA	RT	H	383±3	397±3	5.5±0.7	-	14
		200	H	216±16	221±10	24.2±0.1	-	5
	T6	RT	H	280±7	345±2	15.3±1.7	-	65
	ST + NA (0 h)	RT	H	111±7	244±7	24.9±2.3	-	133
	ST + NA (15 days)	RT	H	190±2	326±1	23.5±0.9	-	136
	ST + NA (30 days)	RT	H	201±6	335±7	22.6±0.7	-	134
E594	As-built	RT	H	316±9	326±5	23.9±1.4	6.7±0.2	10
E66	As-built	RT	H	303±2	321±2	16.2±4.3	4.5±0.2	18
Wrought Al6061	T6	RT	-	276	310	12	-	34

3.3.2 Fracture surface and fracture mechanism

Figure 12 shows the fracture surfaces of the Al6061Mod samples under different conditions. The as-built specimens (Figs. 12a, a_1, and a_2) exhibit dimples while the cleavage fracture near the pores could be occasionally observed. Though the ε_f is lower after DA at 350°C/4h, the fracture surface is still dominated by the ductile dimples (Figs. 12b, b_1, and b_2). After T6 (Figs. 12c, c_1, and c_2) and ST (Figs. 12d, d_1, and d_2), more porosities (as shown by the arrows) were observed because the gas porosities tended to expand during the solution treatment, which has also been reported during ST of L-PBF Al–Si–Mg alloys [64,65]. At the microscale, the fracture surface is dominated by the dimples. When the loading direction is parallel to the building direction, the remnants of laser tracks (Figs. 12e and e_1) are observed from the surface, i.e., the perpendicular laser scanning patterns. Fine dimples at higher magnifications (Figs. 12e$_2$ and e$_3$) suggest the dominant ductile fracture at room temperature.

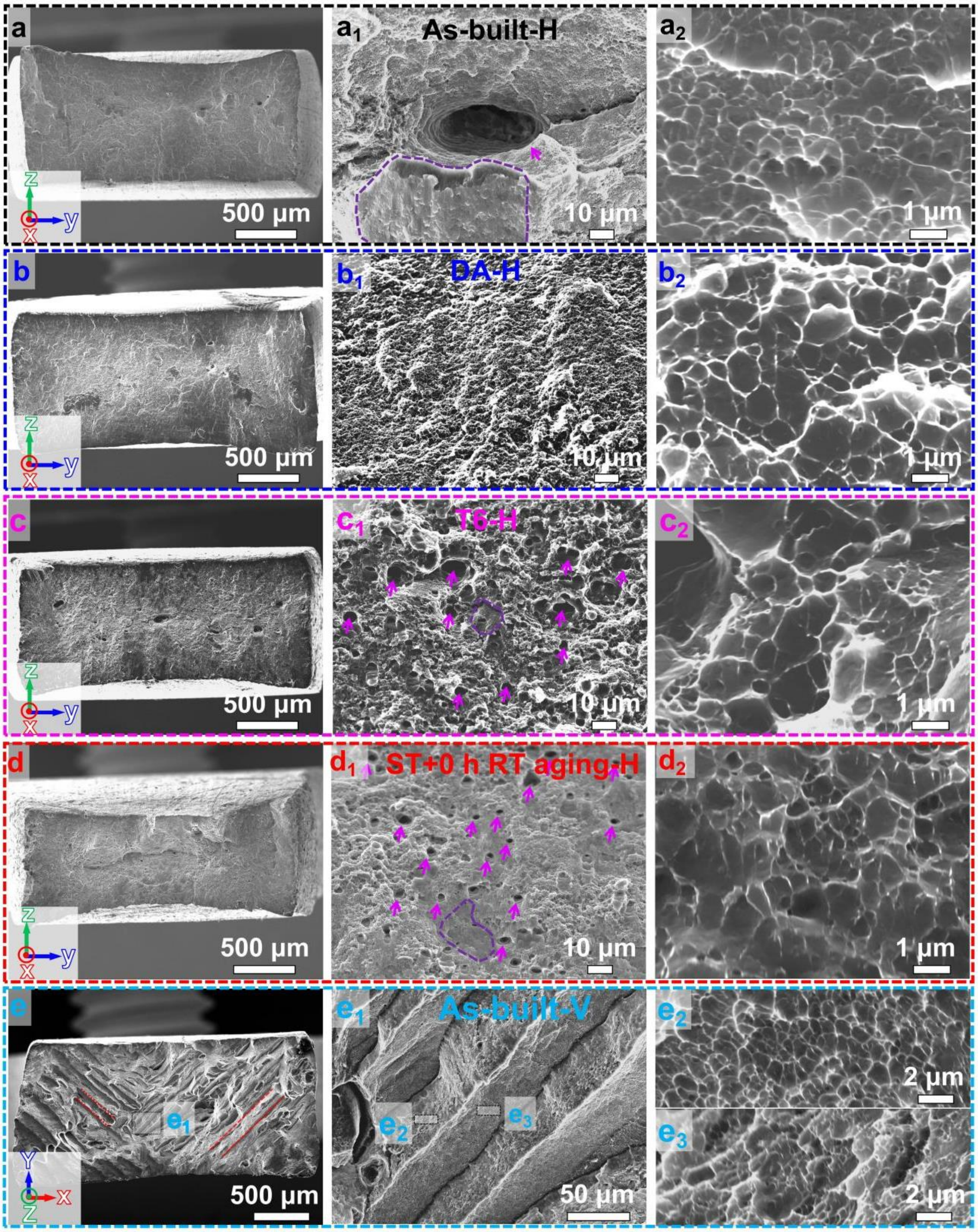

Fig. 12 Fracture surface of L-PBF Al6061Mod with E297 under different conditions. (a) as-built sample in the horizontal direction; (b) DA sample at 350 °C/4h; (c) T6 sample; (d) ST samples; (e) as-built sample in the vertical direction.

4. Discussion

4.1 "Processing-Microstructure" relationship during L-PBF

During the L-PBF process, the interaction between the laser and powders involves multiple physical and chemical phenomena across various length scales [66]. The rapid cooling rate and repeated thermal cycles encourage the formation of non-equilibrium metastable microstructures [67]. Furthermore, the thermal history and cooling rate are spatially different even in a melt pool. It has been calculated that the cooling rate is ~10^6 K/s along the melt pool boundary while it increased to 3×10^7 K/s at the top of melt pools during L-PBF Al6061 [68]. The heterogeneous distribution of cooling rate has also been reported for iron-carbon steel fabricated via L-PBF [69]. The relatively slower cooling rate can leverage the nucleation and growth of $L1_2$-structured primary $Al_3(Sc,Zr)$ particles, providing the heterogeneous nucleation sites and refining the Al matrix grains. However, the enhanced cooling rate towards the center of melt pools can solute trap the Sc and Zr atoms into the matrix, suppressing the formation of primary $Al_3(Sc,Zr)$ particles. Without the primary $Al_3(Sc,Zr)$ particles, the grain growth is assisted with the epitaxial grain growth mode. Such heterogeneous nucleation driven by the primary $Al_3(Sc,Zr)$ particles can also explain the dependence of laser energy density on the microstructure evolution. A lower laser energy density and the concurrent faster cooling rate results in a more significant solute trap of Sc and Zr, leaving fewer primary $Al_3(Sc,Zr)$ to refine the grains, engendering a lower fraction of UFGs [70].

The present work indicates that the laser energy density can effectively tailor the microstructure, such as the multimodal grain size distribution, by influencing the nucleation time for the primary Al_3Sc particles, which are the nucleation sites for the UFGs. Besides the scanning speed, the hatch spacing [71] and the laser remelting [72] have also been adopted to tailor the microstructure of L-PBF Al alloys.

4.2 "Microstructure-Mechanical property" relationship

(i) Mechanical isotropy and heat treatment effect

The as-built Al6061Mod with E297 does not exhibit obvious tensile property anisotropy along the horizontal and vertical directions, since equiaxed UFGs can mitigate the mechanical anisotropy for applications [73]. The as-built Al6061Mod samples exhibit a high ε_f of ~21.1%, in which the Lüders strain constitutes a large portion (~9.3%). The propagation of the Lüders band can be observed from Fig. S4 in the SI. Furthermore, the mechanical property regime of L-PBF Al6061Mod alloy can be extended in a broad window either by tailoring the process parameters or post-heat treatment. Though the laser energy density does not significantly influence the strength, it can alter the deformation behavior as reflected by the Lüders strain (Fig. 10b). The microstructure information enables us to interpret the dependence of laser energy density on the tensile property can be explained from the following perspectives. On the one hand, decreasing the laser energy density can enhance the solute trap of Sc and Zr into the Al matrix, causing a higher contribution from solid solution strengthening. On the other hand, a lower laser energy density leads to a smaller volume fraction of UFGs. The total contribution of laser energy density on the yield strength is the balanced product of solid solution strengthening and grain boundary strengthening. Compared with the tailoring of printing parameters, the heat treatment is more robust in tailoring the yield strength and ductility (Fig. 10d). After solution treatment at 530 °C/5h, the yield strength decreases sharply to ~111 MPa for the samples immediately after solution treatment. However, the solution-treated Al6061Mod is in a metastable non-equilibrium state, and the natural aging can harden the alloy (Fig. 10e). The yield strength is enhanced to ~280 MPa after aging at 175 °C/16 h. As compared with the conventional T6 heat treatment, the direct aging yields a higher yield strength of ~383 MPa. The difference in yield strength is ascribed to the following reasons: (i) For the T6 heat treatment, the grains undergo significant grain coarsening. Meanwhile, the coarsening of $(Al,Si)_3(Sc,Zr)$ particles can deteriorate the yield strength. (ii) For the DA 350 °C/4h sample, the precipitation of nano-sized secondary $Al_3(Sc,Zr)$ particles provides a significant strengthening, enabling a high yield strength. However, the sample does not exhibit work hardening, and strain softening leads to poor plasticity. This indicates that the DA, which is an appropriate heat treatment route for Sc- and Zr-modified Al alloys [50], does not work well for the Sc-and Zr-modified Al6061 alloy. It is necessary to explore more appropriate heat treatment profiles for L-PBF compositionally-modified Al6061 alloys other than direct aging and traditional T6 heat treatment profile due to their specially designed composition and resultant microstructure. It should be noted that the peak-aged Al6061Mod alloy does not engender higher yield strength when tested at 200 °C even though the prevalence of nano-sized $Al_3(Sc,Zr)$ particles. A similar result has been reported for the Al-9Cu-6Ce-1Zr [58] alloy and AlMgZr alloy [40]. It has been rationalized via the coarsening of intermetallic particles at the grain boundaries and the enhanced grain boundary sliding [40]. In the present work, the coarsening of intermetallic particles along the grain boundary is not investigated in detail, and future work needs to be conducted to understand the lack of strengthening for peak-aged Al6061Mod at elevated temperatures.

(ii) Plasticity behavior

Apart from tailoring the strength, the printing parameters and heat treatment influence the deformation behaviors of L-PBF Al6061Mod as well. One specific example is the formation of the Lüders band, which has been commonly observed for the Al alloys with UFGs fabricated with either L-PBF [22,50] or cryo-milling [74], or equal channel angular extrusion (ECAE) [75]. After decreasing the laser energy density from 297 J/mm^3 to 66 J/mm^3 concurrent with a decreased area fraction of UFGs, the Lüders strain drops from ~9.3% to ~4.5%. This can be attributed to the fact that the boundaries of UFGs serve as sinks of dislocations, enhancing the dynamic recovery and reducing the strain hardening [76]. With increasing laser energy density from 297 J/mm^3 to 594 J/mm^3, the reduction of Lüders strain from ~9.3% to ~6.7% is perhaps associated with the higher fraction of UFGs which limits the propagation of the Lüders band, manifesting as a lower Lüders strain. Comparatively, the heat treatment is more robust in tailoring the Lüders strain. For the ST and T6 samples, the Lüders band diminishes due to the grain coarsening to a d_{ave} = 5.3 µm, where the grain boundaries of coarse grains no longer annihilate the dislocations. Relatively, the specimen exhibits work softening after yielding where no Lüders strain is observed for the DA 350 °C/4h, which is attributed to the increased flow stress resulting in the activation of plastic instability [77].

Apart from the Lüders band, obvious serrations were observed called as PLC effect for the Al6061Mod after ST (Fig. 11e), which is due to the interaction between the solute atoms and dislocations [78-81]. After room temperature aging for 15 days, the yield strength increases to ~191 MPa from ~112 MPa for the ST sample due to precipitation of Mg and Zn-enriched phase. Co-currently, the PLC effect diminishes due to the exhaust of solute atoms by forming the Mg-Si-enriched precipitates. When the sample was further room temperature aged for 30 days, the yield strength increased marginally due to slower precipitation kinetics of Mg and Zn in this period (room temperature aging from 16-30 days) relative to that in the first period (room temperature aging from 0-15 days) and 30 days or aging.

5. Conclusion

Crack-free Sc- and Zr- modified Al6061 alloy with a sound printability is additively manufactured by L-PBF. The microstructure and mechanical properties of as-fabricated Al6061Mod samples are tailored in a broad regime by modifying the process parameters and post-heat treatment profiles. The main findings of the present work can be drawn as below:

(1) The L-PBF Al6061Mod samples exhibit multi-modal grains consisting of coarse columnar grains (CCGs) and ultrafine grains (UFGs).

(2) The fraction of UFGs and CCGs of Al6061Mod is influenced by the laser energy density. A higher laser energy density engenders a higher fraction of UFGs, contributed

by a longer time to allow for the precipitation of primary $Al_3(Sc,Zr)$ particles.

(3) The microstructure and mechanical performance of the as-built Al6061Mod can be broadly tailored via post-heat treatment.

(i) Conventional T6 heat treatment triggers the coarsening of grains (grain size of ~ 5.3 µm) and $(Al,Si)_3(Sc,Zr)$ particles (~ 42 nm), resulting in a lower yield strength (~ 280 MPa).

(ii) DA at 350 °C promotes the precipitation of nano-sized $Al_3(Sc,Zr)$ particles (diameter of ~ 5 nm) while maintaining the bimodal grains and grain size, imparting a higher yield strength (~383 MPa) yet work softening.

(iii) DA at 350°C engenders a higher yield strength relative to that of the as-built sample at room temperature. However, the yield strength is similar for DA and as-built samples when tested at 200°C.

Acknowledgement

The financial support from the A*STAR Structural and Metal Alloys Programme (SMAP): Work Package II with project No. A18B1b0061 is acknowledged. The authors acknowledge the assistance of TEM characterization from Dr. Seng Kai Wong and Dr. Rong Ji from the Institute of Materials Research and Engineering (IMRE), A*STAR, Singapore.

Data availability

The data that support the findings of this study are available from the corresponding author upon reasonable request.

References

[1] T. H. Becker, P. Kumar, U. Ramamurty, Fracture and fatigue in additively

manufactured metals, Acta Mater. 2021;219;117240
[2] T. DebRoy, H. L. Wei, J. S. Zuback, T. Mukherjee, J. W. Elmer, J. O. Milewski, A. M. Beese, A. de Wilson-Heid, A. De, W. Zhang, Additive manufacturing of metallic components-process, structure and properties, Prog. Mater. Sci. 2018;92:112-224.
[3] S. Y. Wei, C. Hutchinson, U. Ramamurty, Mesostructure engineering in additive manufacturing of alloys, Scr. Mater. 2023;230:115429.
[4] W. Xu, S. Sun, J. Elambasseril, Q. Liu, M. Brandt, M. Qian, Ti-6Al-4V additively manufactured by selective laser melting with superior mechanical properties, JOM 2015;67:668-673.
[5] K. M. Li, J. J. Yang, Y. L. Yi, X. C. Liu, Y. J. Liu, L. C. Zhang, W. C. Zhang, W. Li, D. C. Chen, S. F. Zhou, Enhanced strength-ductility synergy and mechanisms of heterostructured Ti6Al4V-Cu alloys produced by laser powder bed fusion, Acta Mater. 2023;256:119112.
[6] Y. M. Wang, T. Voisin, J. T. McKeown, J. C. Ye, N. P. Calta, Z. Li, Z. Zeng, Y. Zhang, W. Chen, T. T. Roehling, R. T. Ott, M. K. Santala, P. J. Depond, M. J. Matthews, A. V. Hamza, T. Zhu, Additively manufactured hierarchical stainless steels with high strength and ductility, Nat. Mater. 2018;17:63-71.
[7] J. Radhakrishnan, P. Kumar, S. H. Li, Y. K. Zhao, U. Ramamurty, Unnotched fatigue of Inconel 718 produced by laser bean-powder bed fusion at 25 and 600 °C, Acta Mater. 2022;225 117565.
[8] Y. B. Tang, C. Panwisawas, J. N. Ghoussoub, Y. L. Gong, J. W. G. Clark, A. A. N. Nemeth, D. G. McCartney, R. C. Reed, Alloys-by-design: Application to new superalloys for additive manufacturing, Acta Mater. 2021;202:417-436.
[9] H. Zhang, H. H. Zhu, T. Qi, Z. H. Hu, X. Y. Zeng, Selective laser melting of high strength Al-Cu-Mg alloys: Processing, microstructure, and mechanical properties, Mater. Sci. Eng. A 2016;656:47-54.
[10] Z. H. Hu, X. J. Nie, Y. Qi, H. Zhang, H. H. Zhu, Cracking criterion for high strength Al-Cu alloys fabricated by selective laser melting, Addit. Manuf. 2021;37:101709.
[11] A. Mehta, L. Zhou, T. Huynh, S. Park, H. Hyer, S. T. Song, Y. L. Bai, D. D. Imholte, N. E. Woolstenhulme, D. M. Wachs, Y. H. Sohn, Additive manufacturing and

mechanical properties of the dense and crack free Zr-modified aluminum alloy 6061 fabricated by the laser-powder bed fusion, Addit. Manuf. 2021;41:101966.

[12] J. H. Martin, B. D. Yahata, J. M. Hundley, J. A. Mayer, T. A. Schaedler, T. M. Pollock, 3D printing of high-strength aluminum alloys, Nature 2017;549:365-369.

[13] R. A. Michi, A. Plotkowski, A. Shyam, R. R. Dehoff, S. S. Babu, Towards high-temperature applications of aluminum alloys enabled by additive manufacturing, Inter. Mater. Rev. 2021;67:298-345.

[14] I. M. Kusoglu, B. Gökce, S. Barcikowski, Research trends in laser powder bed fusion of Al alloys within the last decade, Addit. Manuf. 2020;36:101489.

[15] H. Hyer, L. Zhou, A. Mehta, S. Park, T. Huynh, S. T. Song, Y. L. Bai, K. Cho, B. McWilliams, Y. H. Sohn, Composition-dependent solidification cracking of aluminum-silicon alloys during laser powder bed fusion, Acta Mater. 2021;208:116698.

[16] X. P. Li, X. J. Wang, M. Saunders, A. Suvorova, L. C. Zhang, Y. J. Liu, M. H. Fang, Z. H. Huang, T. B. Sercombe, A selective laser melting and solution heat treatment refined Al-12Si alloy with a controllable ultrafine eutectic microstructure and 25% tensile ductility, Acta Mater. 2015;95:74-82.

[17] M. J. Paul, Q. Liu, J. P. Best, X. P. Li, J. J. Kruzic, U. Ramamurty, B. Gludovatz, Fracture resistance of AlSi10Mg fabricated by laser powder bed fusion, Acta Mater. 2021;211:116869.

[18] S. H. Li, Y. K. Zhao, U. Ramamurty, Role of the solidification cells on the yield strength of the Al-Si-Mg alloy manufactured using laser powder bed fusion: A micropillar compression study, Scr. Mater. 2023;234:115566.

[19] Z. G. Zhu, Z. H. Hu, H. L. Seet, T. T. Liu, W. H. Liao, U. Ramamurty, S. M. L. Nai, Recent progress on the additive manufacturing of aluminum alloys and aluminum matrix composites: Microstructure, properties, and applications, Int. J. Mach. Tools Manuf. 2023;190:104047.

[20] S. Z. Uddin, L. E. Murr, C. A. Terrazas, P. Morton, D. A Roberson, R.B. Wicker, Processing and characterization of crack-free aluminum 6061 using high-temperature heating in laser powder bed fusion additive manufacturing, Addit. Manuf. 2018;22:405-415.

[21] A. B. Spierings, K. Dawson, T. Heeling, P. J. Uggowitzer, R. Schäublin, F. Palm, K. Wegener, Microstructural features of Sc- and Zr- modified Al–Mg alloys processed by selective laser melting, Mater. Des. 2017;115:52-63.

[22] Q. B. Jia, P. Rometsch, S. Cao, K. Zhang, X. H. Wu, Towards a high strength aluminum alloy development methodology for selective laser melting, Mater. Des. 2019;174:107775.

[23] K. Kempen, B. Vrancken, S. Buls, L. Thijs, J. Van Humbeeck, J. P. Kruth, Selective laser melting of crack-free high density M2 high speed steel parts by baseplate preheating, J. Manuf. Sci. Eng. 2014;136:061026.

[24] J. H. Martin, B. Yahata, J. Mayer, R. Mone, E. Stonkevitch, J. Miller, M. R. O' Masta, T. Schaedler, J. Hundley, P. Callahan, T. Pollock, Grain refinement mechanisms in additively manufactured nano-functionalized aluminum, Acta Mater. 2020; 200:1022-1037.

[25] Z. G. Zhu, F. L. Ng, H. L. Seet, S. M. L. Nai, Selective laser melting of micron-sized Al7075 alloy: Element evaporation and grain refinement, Mater. Sci. Eng. A 2022;834:142595.

[26] H. Zhang, H. H. Zhu, X. J. Nie, J. Yin, Z. H. Hu, X. Y. Zeng, Effect of zirconium addition on crack, microstructure and mechanical behavior of selective laser melted Al-Cu-Mg alloy, Scr. Mater. 2017;134:6-10.

[27] Q. B. Jia, P. Rometsch, P. Kürnsteiner, Q. Chao, A. J. Huang, M. Weyland, L. Bourgeois, X. H. Wu, Selective laser melting of a high strength Al-Mn-Sc alloy: alloy design and strengthening mechanisms, Acta Mater. 2019;171:108-118.

[28] M. L. M. Sistiaga, R. Mertens, B. Vrancken, X. B. Wang, B. V. Hooreweder, J. P. Kruth, J. V. Humbeeck, Changing the alloy composition of Al7075 for better processability by selective laser melting, J. Mater. Process. Technolo. 2016;238:437-445.

[29] Z. G. Zhu, F. L. Ng, H. L. Seet, W. J. Lu, C. H. Liebscher, Z. Y. Rao, D. Raabe, S. M. L. Nai, Superior mechanical properties of a selective-laser-melted AlZnMgCuScZr alloy enabled by a tunable hierarchical microstructure and dual-nanoprecipitation, Mater. Today 2022;52:90-101.

[30] M. Opprecht, J. P. Garandet, G. Roux, C. Flament, M. Soulier, A solution to the hot cracking problem for aluminum alloys manufactured by laser beam melting, Acta Mater. 2020;197:40-53.

[31] J. R. Croteau, S. Griffiths, M. D. Rossell, C. Leinenbach, C. Kenel, V. Jansen, D. N. Seidman, D. C. Dunand, N. Q. Vo, Microstructure and mechanical properties of Al-Mg-Zr alloys processed by selective laser melting, Acta Mater. 2018;153:35-44.

[32] Q. Y. Tan, H. W. Chang, Y. Yin, F. Wang, D. N. Huang, G. F. Liang, T. Wu, M. Yan, X. Cheng, M. X. Zhang, Simultaneous enhancements of strength and ductility of a selective laser melted H13 steel through inoculation treatment, Scr. Mater. 2022; 219:114874.

[33] K. Schmidtke, F. Palm, A. Hawkins, C. Emmelmann, Process and mechanical properties: Applicability of a Scandium modified Al-alloy for laser additive manufacturing, Phys. Proc. 2011;12:369-374.

[34] https://www.hrl.com/products-services/materials, accessed on 8th, Jan. 2023.

[35] J. Hirsch, Recent development in aluminum alloys for automotive applications, Trans. Nonferr. Met. Soc. China 2014;24:1995-2002.

[36] P. H. Ninive, A. Strandle, S. G. Dahl, W. Lefebvre, C. D. Marioara, S. J. Andersen, J. Friis, R. Holmestad, Ole M. Løvvik, Detailed atomistic insight into the β'' phase in Al–Mg–Si alloys, Acta Mater. 2014;69:126-134.

[37] M. Opprecht, J. P. Garandet, G. Roux, C. Flamnet, An understanding of duplex microstructures encountered during high strength aluminum alloy laser beam melting processing, Acta Mater. 2021;215:117024.

[38] K. V. Yang, Y. J. Shi, F. Palm, X. H. Wu, P. Rometsch, Columnar to equiaxed grains in Al-Mg(-Sc)-Zr alloys produced by selective laser melting, Scr. Mater. 2018;145:113-117.

[39] R. A. Michi, A. Plotkowski, A. Shyam, R. R. Dehoff, S. S. Babu, Towards high-temperature applications of aluminium alloys enabled by additive manufacturing, Int. Mater. Rev, 2022;67:298-345.

[40] S. Griffiths, J. R. Croteau, M. D. Rossell, R. Erni, A. De Luca, N. Q. Vo, D. C. Dunand, C. Leinenbach, Coarsening- and creep resistance of precipitation-strengthened

Al-Mg-Zr alloys processed by selective laser melting, Acta Mater. 2020;188:192-202.

[41] https://www.proterial.com/e/press/2023/pdf/20231030en.pdf, accessed on Dec. 7th, 2023.

[42] Z. H. Hu, S. B. Gao, J. Mikula, X. J. Shen, H. L. Seet, S. S. Quek, K. Zhou, S. M. L. Nai, Enhanced plastic stability: Achieving high performance in a Al6xxx alloy fabricated by additive manufacturing, Adv. Mater., 2024;202307825.

[43] Z. G. Zhu, Q. B. Nguyen, F. L. Ng, X. Z. Liao, P. K. Liaw, S. M. L. Nai, Hierarchical microstructure and strengthening mechanisms of a CoCrFeNiMn high entropy alloy additively manufactured by selective laser melting, Scr. Mater., 2018;154:20-24.

[44] Q. Y. Tan, Z. Q. Fan, X. Q. Tang, Y. Yin, G. Li, D. N. Huang, J. Q. Zhang, Y. G. Liu, F. Wang, T. Wu, X. L. Yang, H. Huang, Q. Zhu, M. X. Zhang, A novel strategy to additively manufacture 7075 aluminum alloy with selective laser melting, Mater. Sci. Eng. A 2022;834:142595.

[45] S. Catchpole-Smith, N. Aboulkhair, L. Parry, C. Tuck, I. A. Ashcroft, A. Clare, Fractal scan strategies for selective laser melting of “unweldable” nickel superalloys, Addit. Manuf. 2017;15:113-122.

[46] H. H. Chen, Y. L. Lo, Y. Y. Hsu, K. L. Lai, Systematic optimization of L-PBF processing parameters for Al alloy 6061 with YSZ nanoparticles, Opt. Laser Technol. 2023;167:109676.

[47] M. Opprecht, G. Roux, J. P. Garandet, C. Flament, A study of the mechanical properties of Al6061-Zr1.2 alloy processed by laser beam melting, J. Mater. Eng. Perform. 2023;32:1840-1855.

[48] K. Strobel, M. A. Easton, L. Sweet, M. J. Couper, J. F. Nie, Relating quench sensitivity to microstructure in 6000 series aluminum alloys, Mater. Trans. 2011;52:914-919.

[49] M. Genc, P. Eloi, J. J. Blandin, C. Pascal, P. Donnadieu, F. De Geuser, P. Lhuissier, C. Desrayaud, G. Martin, Optimization of the strength vs. conductivity trade-off in an aluminium alloy designed for laser powder bed fusion, Mater. Sci. Eng. A 2022;858:144139.

[50] Q. B. Jia, F. Zhang, P. Rometsch, J. W. Li, J. Mata, M. Weyland, L. Bourgeois, M. L. Sui, X. H. Wu, Precipitation kinetics, microstructure evolution and mechanical behavior of a developed Al-Mn-Sc alloy fabricated by selective laser melting, Acta Mater. 2020;193:239-251.

[51] A. Wang, Y. Q. Yan, Z. Y. Chen, H. Z. Qi, Y. Yin, X. H. Wu, Q. B. Jia, Characterisation of the multiple effects of Sc/Zr elements in selective laser melted Al alloy, Mater. Charact. 2022;183:111653.

[52] A. De Luca, D. C. Dunand, D. N. Seidman, Microstructure and mechanical properties of a precipitation strengthened Al-Zr-Sc-Er-Si alloy with a very small Sc content, Acta Mater. 2018;144:80-91.

[53] C. D. Marioara, S. J. Anderson, J. Røyset, O. Reiso, S. G. Dahl, T. E. Nicolasisen, I. E. Opheim, J. F. Helgaker, R. Holmestad, Improving thermal stability in Cu-containing Al-Mg-Si alloys by precipitation optimization, Metall. Mater. Trans. A 2041;45A:2938.

[54] M. J. Yang, H. N Chen, A. Orekhov, Q. Lu, X. Y. Lan, K. Li, S. Y. Zhang, M. Song, Y. Kong, D. Schryvers, Y. Du, Quantified contribution of β'' and β' precipitates to the strengthening of an aged Al-Mg-Si alloy, Mater. Sci. Eng. A 2020;774:138776.

[55] Properties and selection: Nonferrous alloys and special-purpose materials, ASM Handbook, ASM International ed. 1990: 3470.

[56] Z. H. Hu, Y. Qi, X. J. Nie, H. Zhang, H. H. Zhu, The Portevin-Le Chatelier (PLC) effect in an Al-Cu aluminum alloy fabricated by selective laser melting, Mater. Charact. 2021;178:111198.

[57] H. Zhong, P. A. Rometsch, Q. Q. Zhu, L. F. Cao, Y. Estrin, Effect of pre-aging on dynamic strain aging in Al-Mg-Si alloys, Mater. Sci. Eng. A 2017;687:323-331.

[58] S. Bahl, K. Sisco, Y. Yang, F. Theska, S. Primig, L. F. Allard, R. A. Michi, C. Fancher, B. Stump, R. Dehoff, A. Shyam, A. Plotkowski, Al-Cu-Ce(-Zr) alloys with an exceptional combination of additive processability and mechanical properties, Addit. Manuf. 2021;48:102404.

[59] N. E. Uzan, R. Shneck, O. Yeheskel, N. Frage, High-temperature mechanical properties of AlSi10Mg specimens fabricated by additive manufacturing using selective

laser melting technologies (AM-L-PBF), Addit. Manuf. 2018;24:257-263.
[60] A. Plotkowski, K. Sisco, S. Bahl, A. Shyam, Y. Yang, L. Allard, P. Nandwana, A. M. Rossy, R. R. Dehoff, Microstructure and properties of a high temperature Al-Ce-Mn alloy produced by additive manufacturing, Acta Mater. 2020;196:595-608.
[61] R. A. Michi, K. Sisco, S. Bahl, Y. Yang, J. D. Poplawsky, L. F. Allard, R. R. Dehoff, A. Plotkowski, A. Shyam, A creep-resistant additively manufactured Al–Ce–Ni–Mn alloy, Acta Mater. 2022;227:117699.
[62] J. W. Deng, C. Chen, X. C. Liu, Y. P. Li, K. C. Zhou, S. M. Guo, A high-strength heat-resistant Al–5.7Ni eutectic alloy with spherical Al_3Ni nano-particles by selective laser melting, Scr. Mater. 2021;203:114304.
[63] http://www.matweb.com/search/datasheet.aspx?matguid=5b98936d19a54c7ab61223777daa69ae&n=1&ckck=1, accessed on 20th, Oct. 2022.
[64] K. V. Yang, P. Rometsch, D. H. J. Davies, A. J. Huang, X. H. Wu, Effect of heat treatment on the microstructure and anisotropy in mechanical properties of A357 alloy produced by selective laser melting, Mater. Des. 2018;154:275-290.
[65] K. V. Yang, P. Rometsch, T. Jarvis, J. Rao, S. Cao, C. Davies, X. H. Wu, Porosity formation mechanisms and fatigue response in Al-Si-Mg alloys made by selective laser melting, Mater. Sci. Eng. A 2018;712:166-174.
[66] C. Panwisawas, Y. B. Tang, R. C. Reed, Metal 3D printing as a disruptive technology for superalloys, Nat. Commun. 2020;11:2327.
[67] W. Xu, E. W. Lui, A. Pateras, M. Qian, M. Brandt, In situ tailoring microstructure in additively manufactured Ti-6Al-4V for superior mechanical performance, Acta Mater. 2017;125:390-400.
[68] L. E. Loh, C. Chua, W. Yeong, J. Song, M. Mapar, S. Sing, Z. Liu, D. Zhang, Numerical investigation and an effective modeling on the selective laser melting (L-PBF) process with aluminum of 6061, Int. J. Heat Mass Trans. 2015;80:288-300.
[69] Y. C. Wang, J. Shi, Influence of laser scan speed on micron-segregation in selective laser melting of an iron-carbon alloy: A multi-scale simulation study, Procedia Manuf. 2018;26:941-951.
[70] Y. L. Li, D. D. Gu, Parametric analysis of thermal behavior during selective laser

melting additive manufacturing of aluminum powder, Mater. Des. 2014;63:856-867.

[71] Y. S. Ekubaru, O. Gokcekaya, T. Ishimoto, K. Sato, K. Manabe, P. Wang, T. Nakano, Excellent strength-ductility balance of Sc-Zr-modified Al-Mg alloy by tuning bimodal microstructure via hatch spacing in laser powder bed fusion, Mater. Des. 2022;221:110976.

[72] S. Griffiths, M. D. Rossell, J. Croteau, N. Q. Vo, D. C. Dunand, C. Leinenbach, Effect of laser rescanning on the grain microstructure of a selective laser melted Al-Mg-Zr alloy, Mater. Charact. 2018;143:34-42.

[73] C. J. Todaro, M. A. Easton, D. Qiu, D. Zhang, M. J. Bermingham, E. W. Lui, M. Brandt, D. H. StJohn, M. Qian, Grain structure control during metal 3D printing by high-intensity ultrasound, Nat. Commun. 2020;11:142.

[74] B. Q. Han, Z. Lee, D. Witkin, S. Nutt, E. J. Lavernia, Deformation behavior of bimodal nanostructured 5083 Al alloys, Metall. Mater. Trans. A 2005;36A:957.

[75] C. Y. Yu, P. W. Kao, C. P. Chang, Transition of tensile deformation behaviors in ultrafine-grained aluminum, Acta Mater. 2005;53:4019-4028.

[76] D. J. Lloyd, L. R. Morris, Lüders band deformation in a fine-grained aluminum alloy, Acta Metall. 1977;25:857-861.

[77] Y. Z. Tian, S. Gao, L. J. Zhao, S. Lu, R. Pippan, Z. F. Zhang, N. Tsuji, Remarkable transition of yield behaviour and Lüders deformation in pure Cu by changing grain sizes, Scr. Mater., 2018;142:88-91.

[78] H. Aboulfadl, J. Deges, P. Choi, D. Raabe, Dynamic strain aging studied at the atomic scale, Acta Mater. 2015;86:34-42.

[79] H. F. Jiang, Q. C. Zhang, X. D. Chen, Z. J. Chen, Z. Y. Jiang, X. P. Wu, J. H. Fan, Three types of Portevin–Le Chatelier effects: Experiment and modeling, Acta Mater. 2007;55:2219-2228.

[80] P. Zhang, G. Liu, J. Sun, A critical review on the Portevin-Le Chatelier effect on aluminum alloys, J. Cent. South Univ. 2022;29:744-766.

[81] H. F. Jiang, Q. C. Zhang, X. P. Wu, J. H. Fan, Spatiotemporal aspects of the Portevin-Le Chatelier effect in annealed and solution-treated aluminum alloys, Scr. Mater. 2006;54:2041-2045.